

Radiative heat transfer capability implemented in OpenNCC for conjugate heat transfer applications

Makoto Endo, *

NASA John H. Glenn Research Center, Cleveland, Ohio, 44135-3191

Thermal efficiency of gas turbine engine increases as the temperature and pressure at the combustor increases. Consequently, the materials used inside a combustor must survive an increasingly challenging environment. For this reason, accurate assessment of heat transfer is crucial for combustor design. While all three modes of heat transfer are present inside a combustor, the focus of this paper is the thermal radiation. Radiative heat transfer in a gas turbine combustors are particularly interesting from three reasons. Firstly, the radiative heat loss from the combustion region may affect the emission performance. Secondly, the cooling air will protect the liner from convection but not necessary from radiation. Finally, it is less frequently incorporated in CFD analysis than other forms of heat transfer. In this work, radiative heat transfer using discrete ordinate method has been incorporated in OpenNCC (a publicly releasable version of the National Combustion Code) developed at NASA Glenn Research Center. Aside from massively parallel computation capability using MPI and the ability to utilize unstructured mesh, the current implementation includes two types of spectral models, namely, the weighted some of gray gas model and the full spectrum correlated k-distribution model. After presenting the theory and the strategy of implementation, results of validation cases for gray gas and spectral models will be presented. While the implementation of the radiation solver is intended for gas turbine application, the radiation solver can run independently from the convection/combustion solver and the same theory can be applied to other application.

Nomenclature

I	= Radiative intensity [W/m^2]	\mathbf{q}_R	= Radiative heat flux vector [W/m^2]
\hat{a}	= a-factor (see section II)	RQL	= Rich bum - Quick mix - Lean bum
C_{CFL}	= CFL number	RTE	= Radiative Transfer Equation
\mathbf{c}	= Coordinates of the cell centroid, (x_c, y_c, z_c)	s	= Path length for radiation [m]
CHT	= Conjugate Heat Transfer	σ	= Stefan-Boltzmann constant [$W/(m^2K^4)$]
δ	= Small number used to avoid dividing by zero	S_R	= Radiative source term, $-\nabla \cdot \mathbf{q}_R$ [W/m^3]
DO	= Discrete Ordinate	t	= Pseudo time
FSCK	= Full Spectrum Correlated k-distribution	T	= Temperature [K]
κ	= Absorption coefficient [1/m]	w_i	= Weight per spectral equation
\hat{k}	= k-factor (see section II)	w_m	= Weight per angular equation
\mathbf{l}	= Directional cosines, (ξ, μ, η)	WSGG	= Weighted Sum of Gray Gas
LBL	= Line By Line	b	= Subscript to denote black body value
LDI	= Lean Direct Injection	i	= Subscript to denote the spectral index
LES	= Large Eddy Simulation	m	= Subscript to denote the angular index
\mathbf{n}	= Unit normal vector, (n_x, n_y, n_z)	w	= Subscript to denote the wall property
n_c	= Number of angular equations to solve	(x, y, z)	= Coordinates in Cartesian system
n_s	= Number of spectral equations to solve		
\mathbf{w}	= Coordinates of the face centroid at wall, (x_w, y_w, z_w)		

*Research Chemical Engineer, Engine Combustion Branch, Research & Engineering Directorate, M.S. 5-10

I. Introduction

Thermodynamic cycle analysis of gas turbine engine shows that its thermal efficiency increases as the temperature and the pressure at the combustor increases. Consequently, the materials used inside a combustor must survive an increasingly challenging environment. Spatially dependent thermal analysis can lead to effective placement of effusion holes for liner cooling and hence, lead to overall efficiency improvement. In this paper, radiative heat transfer solver is being incorporated in a CFD code with a history of solving combustor simulations to improve its heat transfer capability as well as including the effect of gas phase radiation that may affect the emission performances.

Although it is less frequent to be included in numerical simulations and experimental measurements, the importance of radiative heat transfer within combustors have been reported. Berger et al.[1] studied the sensitivity of an industrial helicopter combustor thermal environment to convection and radiation by means of LES solver, CHT solver and DO radiation solver. They found that the radiation heat fluxes are of the same order of magnitude as the convective heat flux and CHT with radiation are globally in good agreement with experimental thermocolor measurements.

The radiation solver presented in this paper is being incorporated in OpenNCC, which is the open source version of National Combustion Code actively being developed at NASA Glenn Research Center. OpenNCC has been successfully utilized in combustor related simulations for multiple objectives, for instance, LBO limit of alternative fuels in LDI[2], RQL Gas Turbine Combustor[3], and performance analysis of a LDI array[4].

II. Governing Equations and implementation procedure

The equation being solved by the radiation code can be written as follows:

$$\frac{\partial I_{i,m}}{\partial t} = -\frac{\partial I_{i,m}}{\partial s_m} + \hat{\kappa}_i \hat{\alpha}_i I_b - \hat{\kappa}_i I_{i,m} \quad (1)$$

The left-hand side of equation 1 is a pseudo-time-marching term and when the computation reaches steady state, this equation becomes the Radiative Transfer Equation (RTE) without scattering. We will name the two coefficients $\hat{\alpha}$ and $\hat{\kappa}$ as *a-factor* and *k-factor*, respectively. These coefficients are used as place holders for accommodating different spectral models. For example, The full-spectrum correlated k-distribution (FSCK) model will have the $\hat{\kappa}$ to be the *correlation function that relates the reference cumulative k-distribution to the local state* and $\hat{\alpha}$ to be the *black body weight*. The discrete ordinate method is used to convert the RTE from "path of light" to the cartesian coordinate system.

$$\frac{\partial I}{\partial s} = \xi \frac{\partial I}{\partial x} + \mu \frac{\partial I}{\partial y} + \eta \frac{\partial I}{\partial z} \quad (2)$$

The angular resolution and spectral resolution will determine the number of equations to solve. In this paper, we will use the following notation:

$$\begin{aligned} \text{angular resolution: } & 1 \leq m \leq n_c \quad \text{with angular weight of } , w_m \\ \text{spectral resolution: } & 1 \leq i \leq n_s \quad \text{with spectral weight of } , w_i \end{aligned}$$

For heat transfer application, the objective is to compute the divergence of radiative heat flux (radiative heat source) and the radiative wall heat flux.

$$\nabla \cdot \mathbf{q}_R = \sum_{i=1}^{n_s} w_i \hat{\kappa}_i \left(4\pi \hat{\alpha}_i I_b - \sum_{m=1}^{n_c} (w_m I_{i,m}) \right) \quad (3)$$

$$\mathbf{q}_R \cdot \mathbf{n} = \sum_{i=1}^{n_s} w_i \sum_{m=1}^{n_c} (w_m I_{i,m} \cdot \mathbf{n}) \quad (4)$$

A. Boundary conditions

We will only cover the boundary conditions used in this paper, namely, the black wall boundary condition. The current implementation includes periodic BC, symmetry (specular reflection) BC, and conjugate heat transfer BC. When the RTE is solved by the discrete ordinate method, each angle has an inflow and outflow boundary defined as follows:

$$\begin{aligned} \text{Inflow boundary: } & \xi n_x + \mu n_y + \eta n_z < 0 \\ \text{Outflow boundary: } & \xi n_x + \mu n_y + \eta n_z \geq 0 \end{aligned}$$

At the inflow boundary, the wall flux is calculated by the following equation:

$$I_{i,m,w} = \hat{\alpha}_i \epsilon \sigma T_w^4 \quad (5)$$

The wall flux at the outflow boundary may require some attention. When the calculation reaches steady state, equation 1 becomes:

$$\frac{\partial I_{i,m}}{\partial \mathbf{s}_m} = -\hat{\kappa}_i I_{i,m} + \hat{\kappa}_i \hat{\alpha}_i I_b \quad (6)$$

Assuming the medium is homogenous between the wall and the center of the cell that the wall belongs to, equation 6 can be integrated along the path of light as follows:

$$I_{i,m,w} = I_{i,m,\text{cell}} \exp(-\hat{\kappa}_i d) + (\hat{\alpha}_i I_{b,\text{cell}}) (1.0 - \exp(-\hat{\kappa}_i d)) \quad (7)$$

where d is the distance that the light travels. In this paper, d is calculated by the following equation:

$$d = |\mathbf{n} \cdot \mathbf{l}| \frac{(x_w - x_c)n_x + (y_w - y_c)n_y + (z_w - z_c)n_z}{\xi n_x + \mu n_y + \eta n_z} \quad (8)$$

B. Characteristic time scale for the radiation solver

The governing equation 1 has two different time scales, namely, the advection time scale dt_{adv} and the ODE time scale, dt_{ode} . Because we are using discrete ordinate method, the advection velocity is given by the directional cosines.

$$dt_{\text{adv},m} = \min \left(\frac{l_x}{\xi_m}, \frac{l_y}{\mu_m}, \frac{l_z}{\eta_m} \right) \quad (9)$$

The length scale (l_x, l_y, l_z) are calculated as the maximum distance between all the nodes (vertex) of the cell. In order to derive the dt_{ode} , we will consider the governing equation without the advection term:

$$\frac{\partial I}{\partial t} = -\hat{\kappa}_i I + \hat{\kappa}_i \hat{\alpha}_i I_b \quad (10)$$

Although the actual solver utilizes 3-step Runge-Kutta method, we will consider the Euler method for simplicity.

$$\frac{I^{n+1} - I^n}{\Delta t} = -\hat{\kappa}_i I^n + \hat{\kappa}_i \hat{\alpha}_i I_b \quad (11)$$

This equation is equivalent to:

$$\frac{(I^{n+1} - \hat{\alpha}_i I_b) - (I^n - \hat{\alpha}_i I_b)}{\Delta t} = -\hat{\kappa}_i (I^n - \hat{\alpha}_i I_b) \quad (12)$$

Introducing a new variable J such as $J^n = I^n - \hat{\alpha}_i I_b$ will lead to:

$$J^{n+1} = (1 - \hat{\kappa}_i \Delta t) J^n \quad (13)$$

Consequently, the stability condition is:

$$dt_{\text{ode}} = \frac{2}{\hat{\kappa}_i} \geq \Delta t \quad (14)$$

For the radiation solver, the time step size is calculated as the minimum value within the domain per (i, m) , multiplied by a user defined coefficient, C_{CFL} .

$$dt_{i,m} = C_{CFL} \cdot \min(dt_{\text{ode},i}, dt_{\text{adv},m}) \quad (15)$$

C. Spectral models

The WSGG model by Bordbar [5] and FSCK model by Modest [6] has been implemented for testing purposes (not for distribution). Between these two models, the WSGG model has less equations to solve (The value of n_s is five for WSGG and ten for the FSCK) and the evaluation of cell-centered properties ($\hat{\kappa}$ and $\hat{\alpha}$) is found to be quicker. One of the drawbacks of the WSGG model is that the limitation of the range of species concentration. Bordbar et al. listed a summary of different existing formulations of WSGG model developed for high-pressure applicaitons[5]. All the listed WSGG model has some limitation in the molar fraction ratio of H₂O to CO₂, M_r . The model used in the current study has one of the widest range and still, the range of M_r is between 0.1 to 4.0.

D. Numerical methods

The radiation solver and the CFD solver shares the same cell-centered, FVM mesh partitioned by METIS[7]. Communication between each CPUs are handled by non-blocking MPI and the file IOs are performed by noncontiguous collective MPI-IO functions. It should be noted that restarting a radiation calculation requires the radiative intensity per cell, per angular index, per spectral index. Considering that a combustor simulation is likely to be performed with thousands of CPUs, having a fast and reliable IO becomes a nontrivial issue.

Time marching of equation 1 is performed by 3-stage explicit TVD Runge–Kutta scheme[8] that does not require an intermediate solutions to be stored. There are two types of residuals to determine the convergence of equation 1:

$$R_1 = \sum_{i_{\text{cell}}=1}^{N_{\text{cell}}} \left(\frac{|I_{i,m}^{n+1} - I_{i,m}^n|}{\max(I_{i,m}^{n+1}, \delta)} \right)_{i_{\text{cell}}} \quad (16)$$

$$R_2 = \sum_{i_w=1}^{N_w} \left(\frac{|I_{i,m}^{n+1} - I_{i,m}^n|}{\max(I_{i,m}^{n+1}, \delta)} \right)_{i_w} \quad (17)$$

The computation is considered converged when R_1 is below a prescribed value for all angles (m) and R_2 is below a prescribed value as well. When the calculation involves reflection (including symmetric BC), the outflow boundary value of one angle becomes the inflow boundary of another angle and hence, the necessity to check the convergence of wall values rises.

The accuracy and computational load of discrete ordinate method can be adjusted by the selection of the quadrature sets. The radiation solver is capable of reading user-defined quadrature set as well as some built-in options. Results included in this paper are all obtained using the T4 quadrature set by Thurgood[9], which has 128 direction in three dimensional space.

III. Validation Problems:

The following subsections will go over the performance of the radiation solver by solving various validation problems. In general, studies on numerical radiative heat transfer can roughly be divided into two parts. The first part is how to solve the RTE accurately in multi-dimensions by dealing with angular and numerical discretizaion. The second part is how to incorporate the effect of participating media. These two parts are validated in subsections III.A and III.B, respectively. For engineering application, being able to handle unstructured mesh is a highly desirable feature. The third subsection(III.C) will cover this capability.

A. Gray gas

This section will focus on gray-gas validation problem to check the accuracy associated with angular and numerical discretizaion. We will solve for the wall heat flux along the centerline of a bottom wall in a cubic enclosure[10]. Edges of the cube is 1m and it is filled with gas with uniform temperature. All walls are cold and black. Calculation is performed for three different absorption coefficients, namely, 0.1, 1.0 and 10.0 [1/m]. Figure 1 shows the uniform mesh of 25x25x25 cells that is being used. Figure 2 shows the comparison against the exact solution. It can be seen that the wall heat flux (non-dimensionalized by σT^4) is well-aligned with the exact solution.

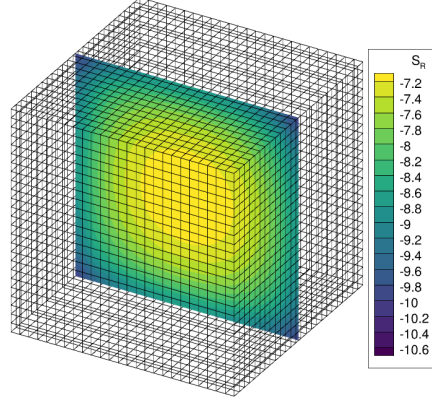


Fig. 1 Uniform mesh used for gray-gas validation
(The contour shows the non-dimensional S_R for $\kappa = 1.0$)

B. Non-Gray gas

This section will focus on non-gray-gas validation problem to check the accuracy associated with the modeling of participating media. The test cases are similar to the cases proposed by Liu [11] with the validation data obtained from Fraga et al.[12] and Porter et al.[13]. The geometry is a 2m x 2m x 4m rectangular enclosure at 1atm and the temperature distribution are shown in figure 3. All walls are black and at a uniform temperature of 300 K. The participating species are CO_2 and H_2O with molar concentrations shown in table 1. The calculation was executed using 20CPUs on ivy bridge

Table 1 Species concentration for non-gray test problem

case number	$x_{\text{H}_2\text{O}}$	x_{CO_2}	source
1	0.2	0.1	case 3 of Fraga et al. [12]
2	flame shaped distribution	$x_{\text{H}_2\text{O}}/2$	case 4 of Fraga et al. [12]
3	0.10	0.85	case 3 of Porter et al. [13]

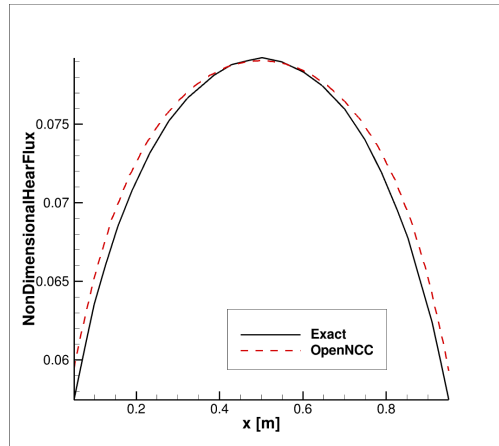
machines on NASA Advanced Supercomputing (NAS) facility[14]. Table 2 compares the calculation time between the two spectral models. It should be noted that calculation time can depend on many factors not limited to the model

Table 2 Computation time comparison using 20CPUs on ivy (units in seconds)

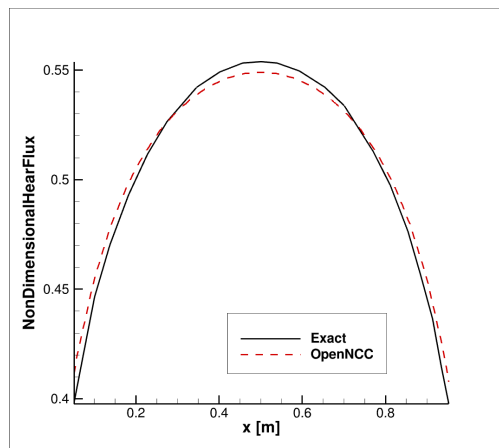
model	case1		case2		case3	
	FSCK	WSGG	FSCK	WSGG	FSCK	WSGG
run#1	657	74	644	73	698	73
run#2	651	73	639	73	683	73

formulation. The computation time listed on table 2 is only applicable to the current implementation. Radiative source term along the center line ($x=0,y=0$) and wall heat flux along the center of the side wall ($x=0,y=-1$) is compared against LBL solutions in figure4, 5 and 6.

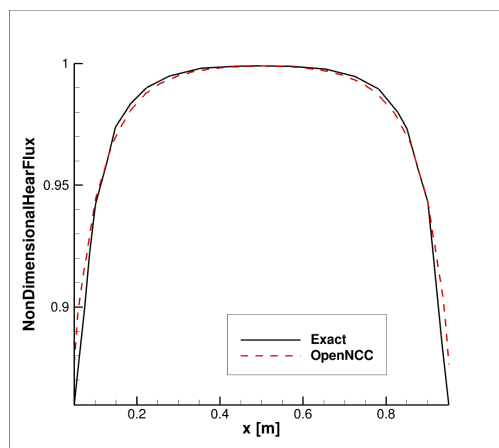
From figure 4 and 5, it can be seen that both spectral models are capturing the overall trend of radiative source term and wall heat flux. In both cases, the source term calculated by the FSCK model is slightly higher than the LBL model value and the WSGG model value is lower than the LBL model for most regions.. For the wall heat flux, the FSCK model value is higher than the LBL model value and the WSGG model value is lower than the LBL model value. Contrary to the other two cases, case3 has more CO_2 than H_2O . From the results plotted in figure 6, it can be seen that despite the change in the species concentration, the relationship between the FSCK model and the WSGG model is being maintained. It should also be noted that the wall heat flux value of the FSCK model is close to the LBL value and the peak value is larger than the LBL model value. Table3 compares the difference in the maximum wall heat flux per



(a) Comparison of wall heat flux: $\kappa = 0.1$



(b) Comparison of wall heat flux: $\kappa = 1.0$



(c) Comparison of wall heat flux: $\kappa = 10.0$

Fig. 2 Wall heat flux along the centerline of a bottom wall in a cubic enclosure

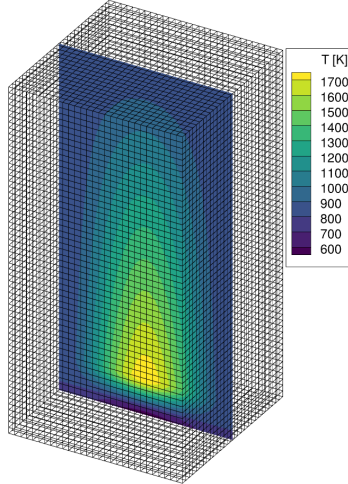


Fig. 3 Non-gray, uniform mesh, 49,619 cells (29x29x59)

spectral model for the three cases. The maximum wall heat flux value differed in the range of -7% to +15% that could

Table 3 Difference in the maximum wall heat flux compared to the LBL value

	case1	case2	case3
FSCK	-7.0%	-6.9%	+2.1%
WSGG	+6.9%	+17.2%	+7.0%

become concerning depending on the required level of accuracy. It should be noted that by running two spectral models for the same problem, the solutions can be used as a guideline to estimate the true value.

C. Non-Uniform mesh

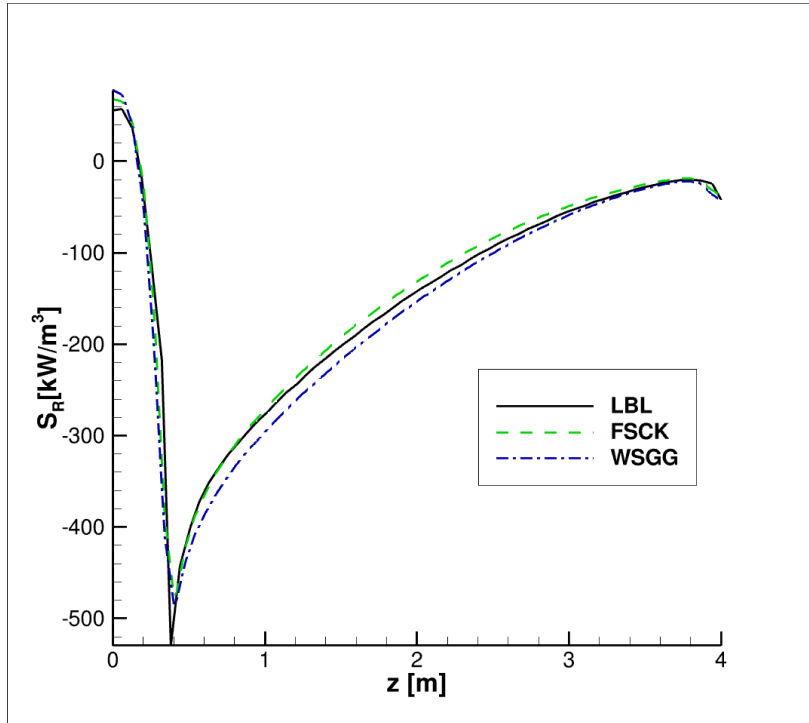
This section will focus on the performance of the radiation solver when it is applied to non-uniform (unstructured) mesh. The geometry used in this section is a 2m x 2m x 4m rectangular enclosure, identical to the geometry used in section III.B. Figure 7 shows the non-uniform mesh used in this section. One of the mesh consists of all tetrahedral elements (7a) and the other mesh has five layers of expanding prisms with minimum wall distance of 1cm (7b). Table 4 compares the number of cells used in each of the four meshes used in this section. The number of cells increases in the order of coarse uniform mesh, non-uniform all tetrahedral mesh, dense uniform mesh, and non-uniform mixed elements mesh.

Table 4 Number of cells in each mesh

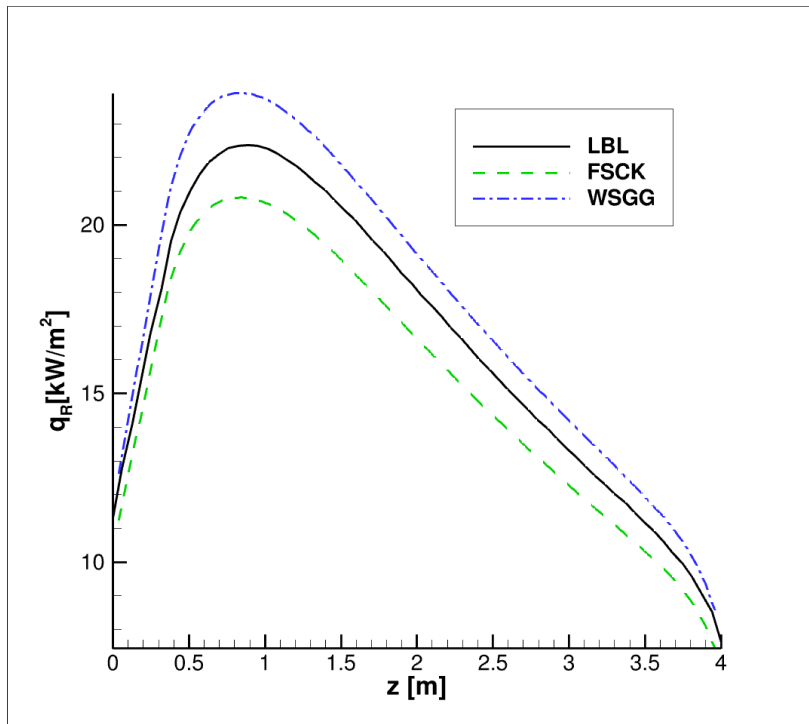
Name of the mesh	Number of cells
Uniform-coarse (29x29x59)	49,619
Uniform-dense (59x59x119)	414,239
Non-uniform all tetrahedelon	309,722
Non-uniform mixed elements	793,297

Figure 8 compares the performance against gray gas problem. The uniform gas temperature, wall temperature, and the absorption coefficient are 1000K, 300K, and 1.0 [1/m], respectively. It can be seen from figure 8 that all four meshes are providing similar results in both, radiative source term and the wall heat flux. The results of the coarse uniform mesh is slightly away from the other three cases due to the resolution.

Figure 9 and 10 compares the performance against non-gray gas problem. While both figures show the results of

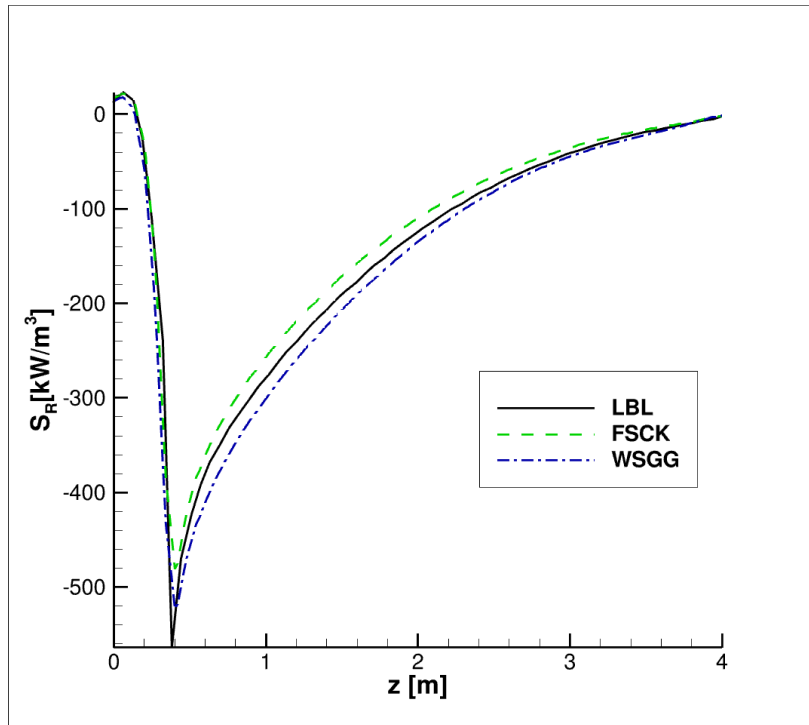


(a) comparison of radiative source term

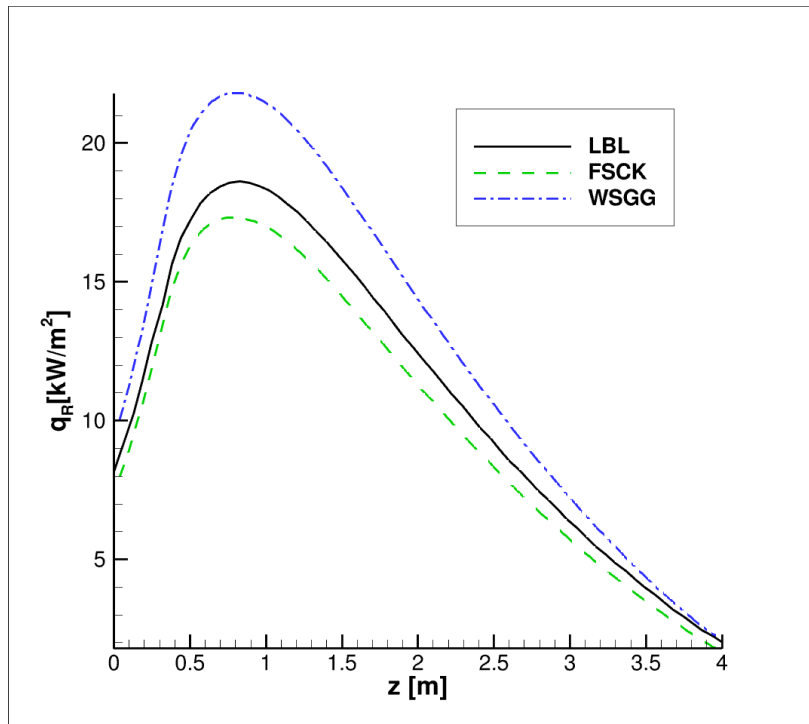


(b) comparison of wall heat flux

Fig. 4 Comparison of case1, LBL data from Fraga et al.[12]

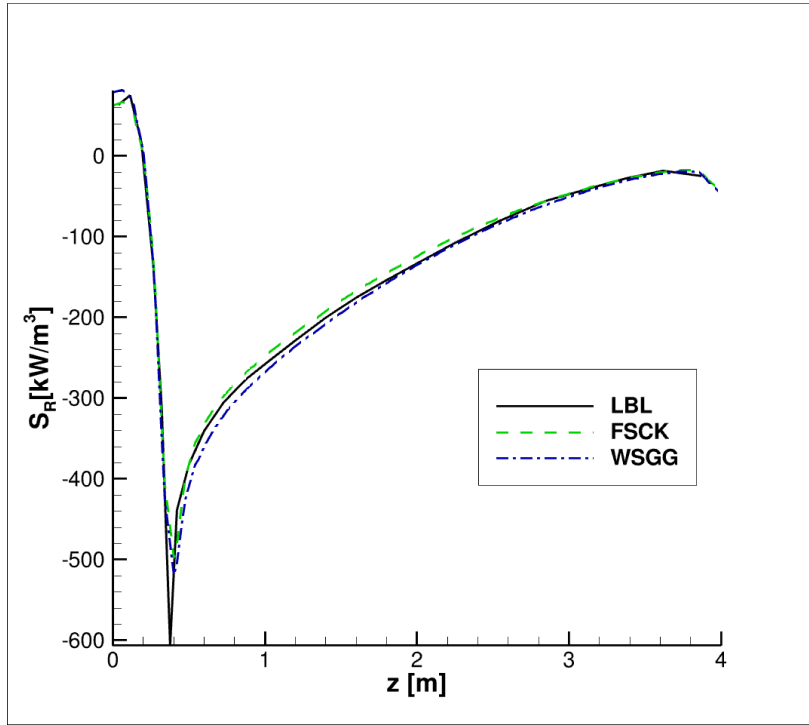


(a) comparison of radiative source term

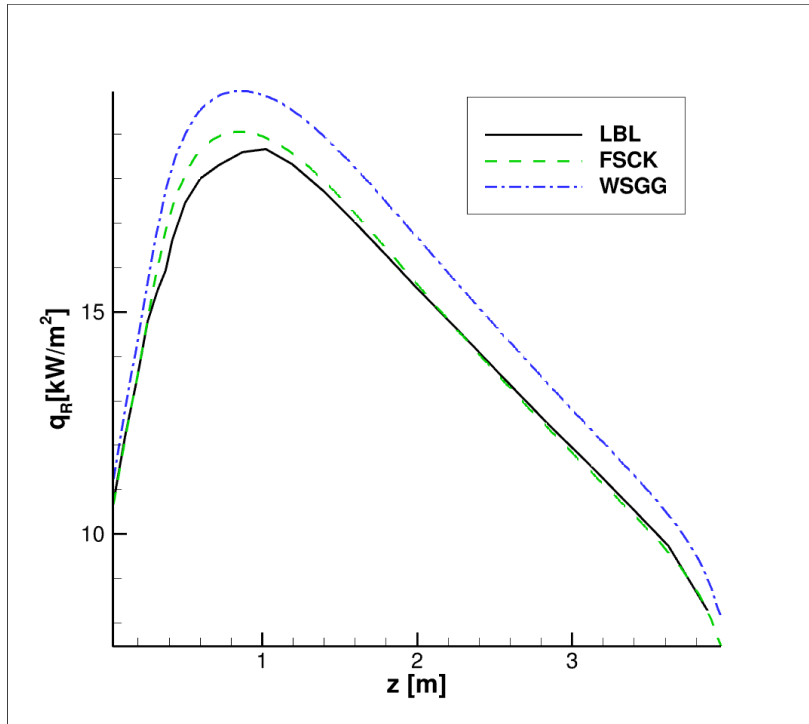


(b) comparison of wall heat flux

Fig. 5 Comparison of case2, LBL data from Fraga et al.[12]



(a) comparison of radiative source term



(b) comparison of wall heat flux

Fig. 6 Comparison of case3, LBL data from Porter et al.[13]

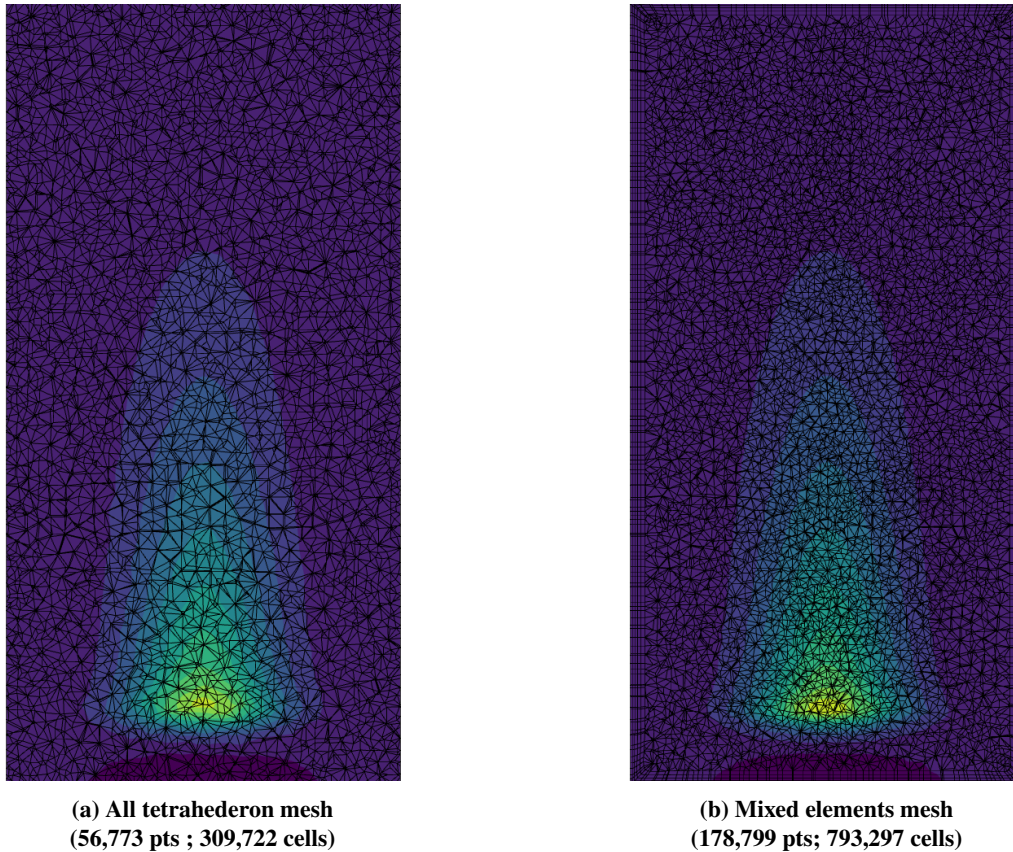
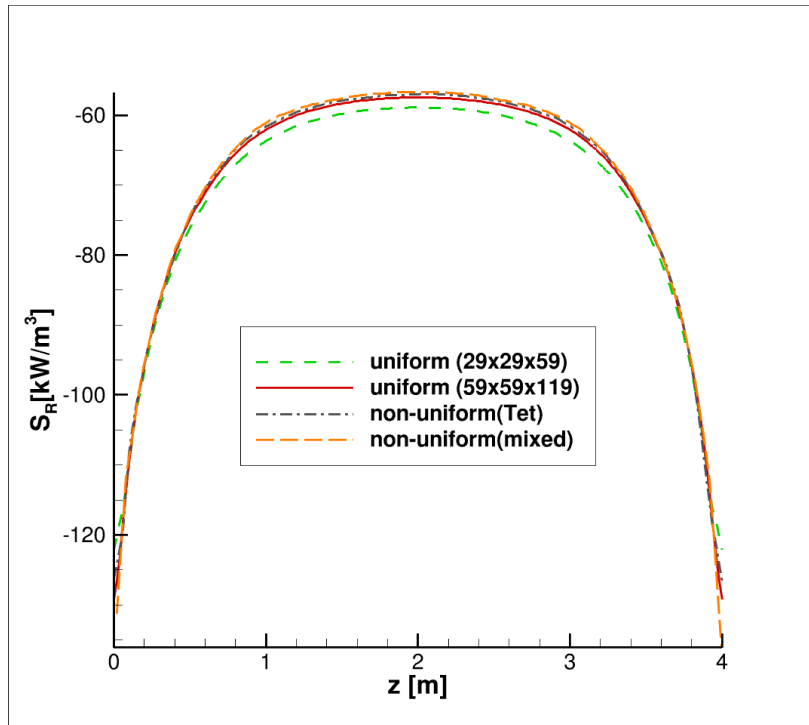


Fig. 7 Non-uniform mesh distribution compared at the center cut-plane ($x=0$)

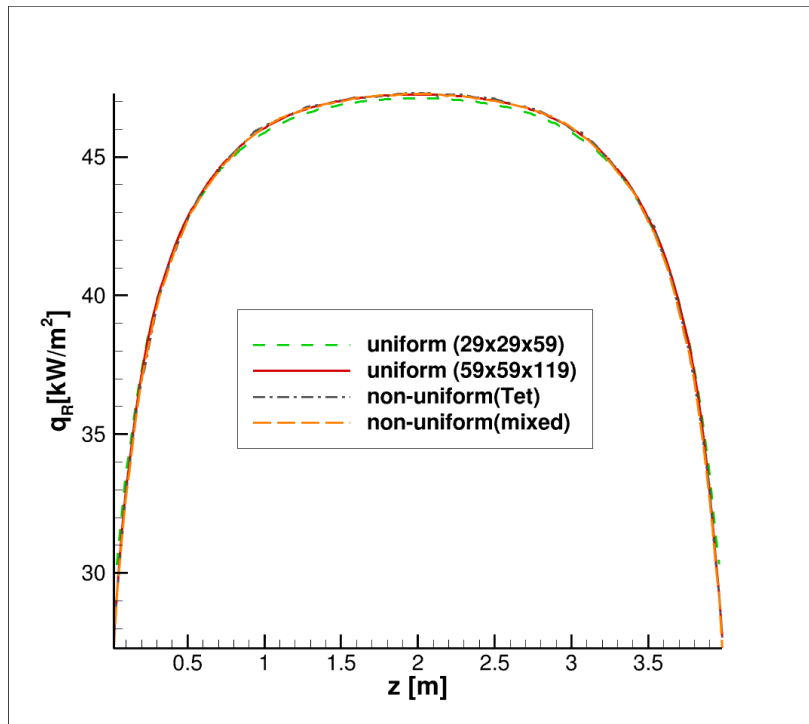
solving case2 of table1, the spectral model being used are FSCK model and WSGG model, respectively. Despite the difference in the spectral model, these two figures show that the all-tetrahedron mesh and the mesh with mixed elements presents similar results expect that the oscillation in the wall heat flux gets removed with the mixed elements mesh that has a layer of uniformly distanced cells near the wall. While the radiative source terms looks similar for all four meshes, some differences can be observed in the radiative wall heat flux. Interestingly, as the resolution of the uniform mesh increases, the wall heat flux values are becoming closer to the non-uniform mesh solutions. This could be a combined effect of the choice of quadratures set (respect to the mesh orientation) and how well the species/temperature distribution is captured by the mesh.

IV. Summary

The theory and the implementation of the newly developed radiative heat transfer capability added to OpenNCC has been explained and its performance has been presented through series of validation problems. The results of solving the gray gas problem matched well with the theoretical solution, indicating that the current solver has a sufficient accuracy associated with spatial discretization. The non-gray gas computations were performed for flame shaped temperature distribution using FSCK and WSGG spectral models with CO_2 and H_2O as participating media. Three different species concentration were considered and both spectral models were able to capture the characteristic of the referenced LBL solution for all cases. While there may be some concerns in the absolute value of the heat flux depending on the required accuracy, both models are likely to discover the region that gets most/least radiative heat flux. The last set of calculations were performed using non-uniform (unstructured) mesh and it was shown that current solver can be reliable in this situation. Similarly to the case involving convection/conduction, having a uniformly-distanced cells near the wall was shown to be helpful to resolve the heat flux in a smooth manner. This solver is expected to be combined with other capabilities of OpenNCC and applied to a realistic engineering problem.

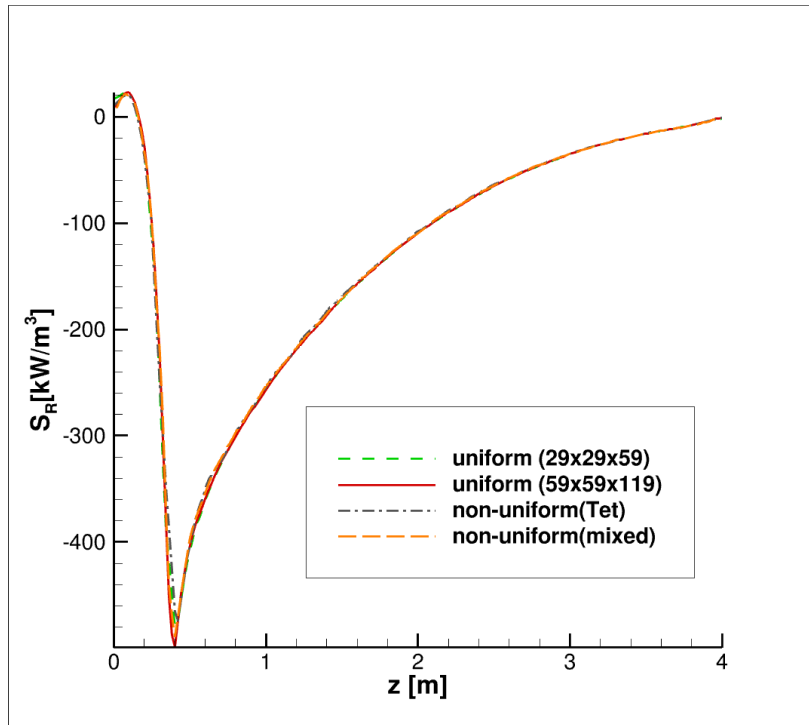


(a) comparison of radiative source term

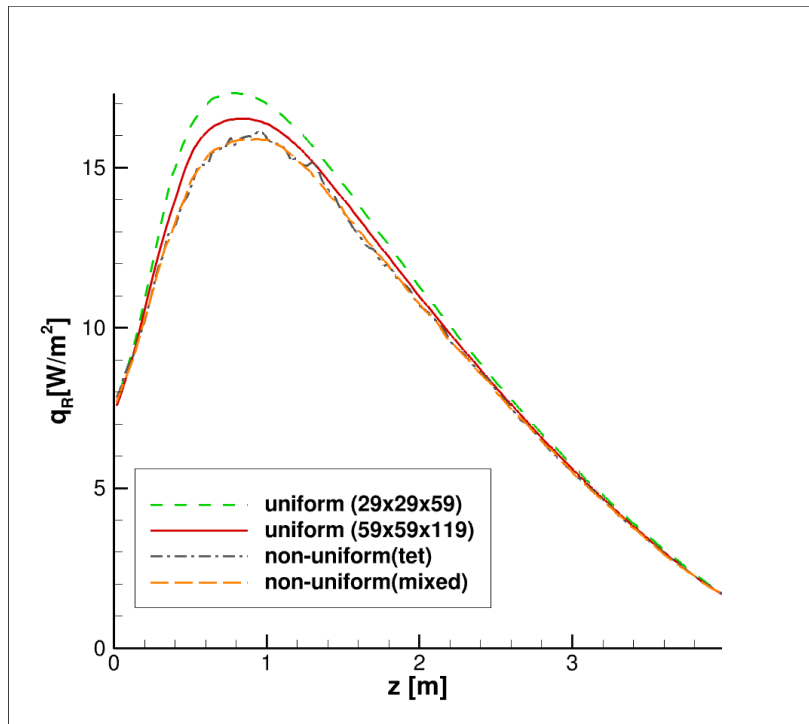


(b) comparison of wall heat flux

Fig. 8 Comparison of effect of mesh types: gray gas ($\kappa=1.0$, $T=1000\text{K}$, $T_w=300\text{K}$)

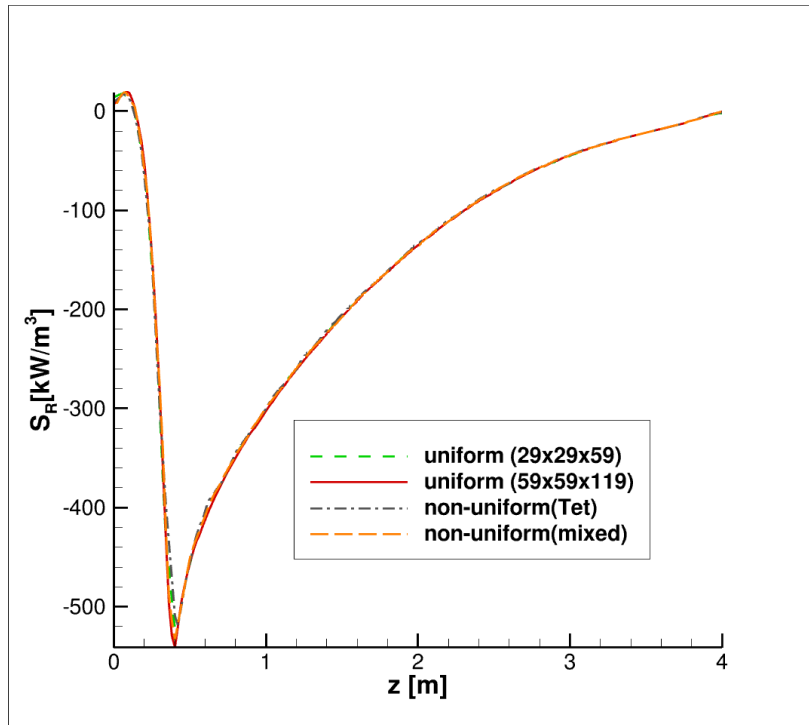


(a) comparison of radiative source term

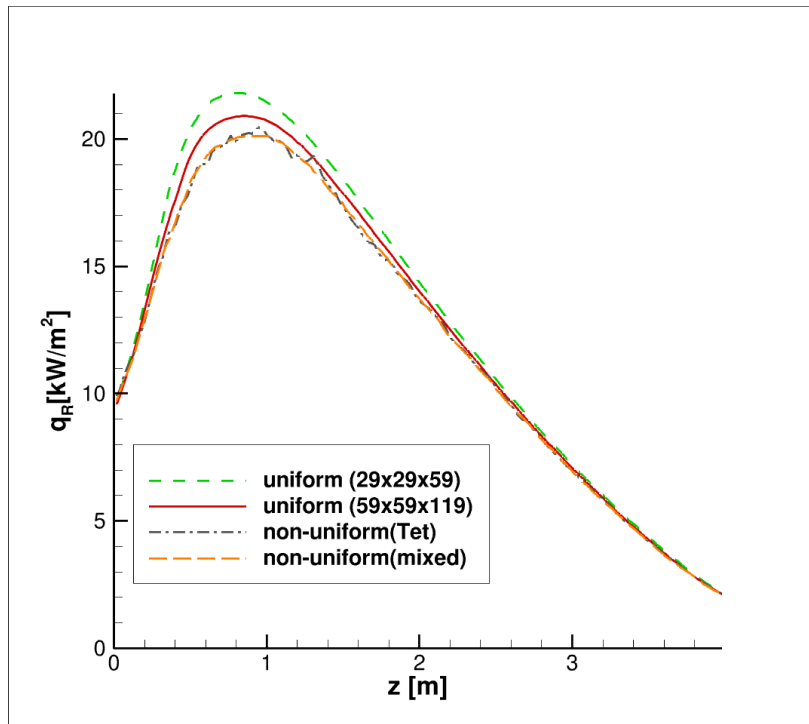


(b) comparison of wall heat flux

Fig. 9 Comparison of effect of mesh types: case2 of table1 using FSCK



(a) comparison of radiative source term



(b) comparison of wall heat flux

Fig. 10 Comparison of effect of mesh types: case2 of table1 using WSGG

Acknowledgments

This work was supported by the NASA Transformational Tools and Technologies Project. Resources supporting this work were provided by the NASA High-End Computing (HEC) Program through the NASA Advanced Supercomputing (NAS) Division at Ames Research Center.

References

- [1] Berger, S., Richard, S., Duchaine, F., Staffelbach, G., and Gicquel, L., “On the sensitivity of a helicopter combustor wall temperature to convective and radiative thermal loads,” *Applied Thermal Engineering*, Vol. 103, 2016, pp. 1450–1459. <https://doi.org/https://doi.org/10.1016/j.applthermaleng.2016.04.054>, URL <https://www.sciencedirect.com/science/article/pii/S1359431116305403>.
- [2] Endo, M., Tacina, K. M., Hicks, Y. R., Capil, T., and Moder, J. P., “Numerical Simulation of Lean Blowout of Alternative Fuels in 7-element Lean Direct Injector,” *AIAA Propulsion and Energy 2021 Forum*, American Institute of Aeronautics and Astronautics, 2021. <https://doi.org/10.2514/6.2021-3458>, URL <https://arc.aiaa.org/doi/abs/10.2514/6.2021-3458>.
- [3] Wey, C. T., “Fuel Sensitivity of Lean Blowout in a RQL Gas Turbine Combustor,” *AIAA Propulsion and Energy 2019 Forum*, American Institute of Aeronautics and Astronautics, 2019, p. 170. <https://doi.org/10.2514/6.2019-4035>, URL <https://arc.aiaa.org/doi/abs/10.2514/6.2019-4035>.
- [4] Ajmani, K., Lee, P., Chang, C. T., and Tacina, K. M., “Pilot Injector Redesign to Reduce N+3 Cycle Emissions For A Gas-Turbine Combustor,” *AIAA Propulsion and Energy 2019 Forum*, American Institute of Aeronautics and Astronautics, 2019. <https://doi.org/10.2514/6.2019-4371>, URL <https://arc.aiaa.org/doi/abs/10.2514/6.2019-4371>.
- [5] Bordbar, H., Coelho, F. R., Fraga, G. C., França, F. H., and Hostikka, S., “Pressure-dependent weighted-sum-of-gray-gases models for heterogeneous CO₂-H₂O mixtures at sub- and super-atmospheric pressure,” *International Journal of Heat and Mass Transfer*, Vol. 173, 2021, p. 121207. <https://doi.org/https://doi.org/10.1016/j.ijheatmasstransfer.2021.121207>, URL <https://www.sciencedirect.com/science/article/pii/S0017931021003100>.
- [6] Modest, M. F., “Spectral Radiation Calculation Software (SRCS),” provided by M. F. Modest to NASA Glenn Research Center under NASA Grant NNX07AB40A, 2008.
- [7] Karypis, G., and Kumar, V., “METIS: A Software Package for Partitioning Unstructured Graphs, Partitioning Meshes, and Computing Fill-Reducing Orderings of Sparse Matrices,” Retrieved from the University of Minnesota Digital Conservancy, 1997. URL <https://hdl.handle.net/11299/215346>.
- [8] Gottlieb, S., and Shu, C.-W., “Total variation diminishing Runge-Kutta schemes,” *Mathematics of Computation*, Vol. 67, No. 221, 1998, pp. 73–85.
- [9] Thurgood, C., “A critical evaluation of the discrete ordinates method using HEART and Tn quadrature,” Ph.D. thesis, Queen’s University, Kingston, Canada, 1992.
- [10] Kang, S. H., and Song, T.-H., “Finite element formulation of the first- and second-order discrete ordinates equations for radiative heat transfer calculation in three-dimensional participating media,” *Journal of Quantitative Spectroscopy and Radiative Transfer*, Vol. 109, No. 11, 2008, pp. 2094–2107. <https://doi.org/10.1016/j.jqsrt.2008.02.016>.
- [11] Liu, F., “Numerical Solutions of Three-Dimensional Non-Grey Gas Radiative Transfer Using the Statistical Narrow-Band Model,” *Journal of Heat Transfer*, Vol. 121, No. 1, 1999, pp. 200–203. <https://doi.org/10.1115/1.2825944>, URL <https://doi.org/10.1115/1.2825944>.
- [12] Fraga, G. C., Bordbar, H., Hostikka, S., and França, F. H. R., “Benchmark Solutions of Three-Dimensional Radiative Transfer in Nongray Media Using Line-by-Line Integration,” *Journal of Heat Transfer*, Vol. 142, No. 3, 2020. <https://doi.org/10.1115/1.4045666>, URL <https://doi.org/10.1115/1.4045666>, 034501.
- [13] Porter, R., Liu, F., Pourkashanian, M., Williams, A., and Smith, D., “Evaluation of solution methods for radiative heat transfer in gaseous oxy-fuel combustion environments,” *Journal of Quantitative Spectroscopy and Radiative Transfer*, Vol. 111, No. 14, 2010, pp. 2084–2094. <https://doi.org/https://doi.org/10.1016/j.jqsrt.2010.04.028>, URL <https://www.sciencedirect.com/science/article/pii/S0022407310001652>.
- [14] “Pleiades Configuration Details,” Online, Retrieved Jul21, 2023. URL https://www.nas.nasa.gov/hecc/support/kb/pleiades-configuration-details_77.html.